IRAQI JOURNAL OF MATERIALS
Volume (1) Issue (1) January-March 2022, pp. 25-38

Employment of Closed-Field Dual Magnetrons Sputtering for Synthesis of Silicon Nitride Nanostructures

Firas J. Kadhim [1], Mohammed K. Khalaf [2], Oday A. Hammadi [3]

[1] *Department of Physics, College of Science, University of Baghdad, Baghdad, IRAQ*
[2] *Ministry of Science and Technology, Baghdad, IRAQ*
[3] *Department of Physics, College of Education, Al-Iraqia University, Baghdad, IRAQ*

Abstract
In this work, novel design of closed-field unbalanced dual magnetrons system was employed in a DC reactive sputtering system to prepare silicon nitride nanostructures. Two types of silicon wafers (n- and p-type) were sputtered in presence of nitrogen gas to deposit nanostructured silicon nitride thin films on glass substrates. The prepared nanostructured were polycrystalline with six dominant crystal planes: (101), (110), (200), (232), (301) and (321). The surface roughness of the sample prepared at inter-electrode distance of 4cm was higher than other samples prepared at smaller or larger distances and the average and R.M.S roughness were 0.777 and 1.03 nm, respectively. The nanoparticles of minimum size of 30nm were formed and recognized as individual accumulated particles. Two bands of significant absorption were observed around 960 and 1086 cm^{-1}, those are attributed to the Si-N-Si vibration mode in Si_3N_4 molecule. An absorption peak was observed at 389nm, which is attributed to the quantum size effect of nanostructures. The refractive index of the prepared Si_3N_4 samples was determined to be 1.38-2.1 and the energy band gap was ranging in 5.1-5.2 eV. The energy band gap was found to increase with decreasing thickness of the prepared film. The wide energy band gap of Si_3N_4 nanostructures makes them good candidate, as similar as AlN, BN and GaN, for power electronics and optoelectronics operating at high temperatures.

***Keywords*:** Silicon nitride; Nanostructures; Reactive sputtering; Magnetron sputtering
Received: 4 August 2021; **Revised:** 11 November; **Accepted:** 18 November; **Published:** 1 January 2024

1. Introduction

Silicon nitride (Si_3N_4) was developed in the 1960s and 1970s in a search for fully dense, high strength and high toughness materials [1]. A prime driver for its development was to replace metals with ceramics in advanced turbine and reciprocating engines for higher operating temperatures and efficiencies [2,3].

Silicon nitride is a polymorphic material, presenting three crystallographic modifications designated as the α, β and γ phases [4]. The α and β phases can be produced under normal nitrogen pressure and have great importance in the production of advanced ceramics, while the recently discovered γ-Si_3N_4 can be formed only at extremely high pressures and has no practical use yet [4,5].

In a simple chemical picture, chemical bonding in α-Si_3N_4 and β-Si_3N_4 is due to the overlap of the **sp^3** hybrid orbitals of silicon atoms with the **sp^2** hybrid orbitals of the nitrogen atoms [6]. Each nitrogen atom has a remaining **p** nonbonding atomic orbital that is occupied by a single pair of electrons [7]. The □-Si_3N_4 and □-Si_3N_4 have trigonal and hexagonal structures, respectively, which are built up by corner-sharing SiN_4 tetrahedra [7,8]. The cubic γ-Si_3N_4 is often designated as “c” modification in the literature, in analogy with the cubic modification of boron nitride (c-BN) [9]. Table (1) shows a comparison of crystal information of □-Si_3N_4 and □-Si_3N_4 with other crystal structures.

The basic unit of Si_3N_4 is the SiN_4 tetrahedron. A silicon atom is located at the center of a tetrahedron, with four nitrogen atoms at each corner [10]. The SiN_4 tetrahedra are joined by sharing corners in such a manner that each nitrogen atom is common to three tetrahedra. Thus, nitrogen has three silicon atoms as neighbors [4,11]. The structural difference between α-Si_3N_4 and β-Si_3N_4 can be explained by different arrangements of Si-N layers, as seen in Fig. (1). The basic units are linked

 ISSN (print) 2958-8960 (online) xxxx-xxxx Printed in IRAQ

together to form wrinkled or puckered six-membered rings which surround large holes. These basal planes form the building blocks for the structures of α-Si_3N_4 and β-Si_3N_4 [12].

Table (1) Crystal information of α-Si_3N_4 and β-Si_3N_4 with other crystal structures [9-12]

Crystal	α-Si_3N_4	β-Si_3N_4	α-SiO_2	Si_2N_2O
Lattice constant (Å)				
a:	7.766	7.586	4.913	8.843
b:				5.437
c:	5.615	2.902	5.405	4.835
Space group	Hexagonal	Hexagonal	Hexagonal	Orthorhombic
Bond distance (Å)				
Si-N (average)	1.738	1.730		1.714
Si-O (average)			1.610	1.623
Bond angle				
Si-N-Si	118.8	119.9		8120
Si-O-Si			144	147.4

Silicon nitride (Si_3N_4) has the strongest covalent bond properties next to silicon carbide [13]. Its optical and electrical properties at nanoscale are encouraging to fabricate photonic devices by depositing nano films of Si_3N_4 on semiconducting substrates [14]. At room temperature, it has high resistivity (~10^{13} □.cm), dielectric constant of 7.0 and wide energy gap of 5.06-5.25 eV [15].

Silicon nitride (Si_xN_y) thin films are common insulators in the semiconductor industry for the passivation of electronic devices because they form excellent protective barriers against the diffusion of water, sodium and potassium ions found in biological environments [16,17]. The Young's modulus of silicon nitride thin film is higher than that of silicon and its intrinsic stress can be controlled by the specifics of the deposition process [18,19]. Silicon nitride is an effective masking material in many alkaline etch solutions [20].

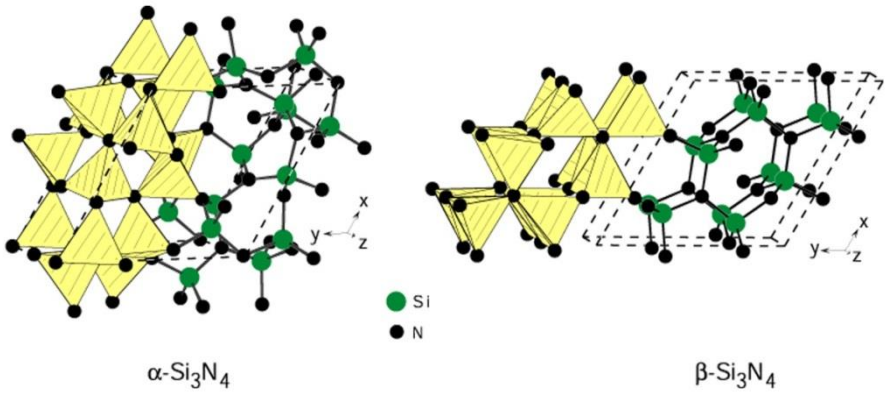

Fig. (1) Crystal structures of trigonal α-Si_3N_4 and hexagonal β-Si_3N_4, emphasizing the corner-sharing SiN_4 tetrahedra [2]

Silicon nitride (Si_3N_4) is widely used as hard optical material but also has excellent piezoelectric response [21]. In addition to their numerous optical applications, silicon nitride (Si_3N_4 or $SiN_{1.3}$) thin films have applications in surface passivation for microcrystalline silicon solar cells, high frequency piezoelectric transducers, biomedical applications and in nanocomposites [22-25].

2. Experimental Part

The magnetron sputtering system used in this work was designed to include vacuum chamber, discharge electrodes and magnetron assembly, vacuum unit, dc power supplies, gas supply system, cooling system and measuring instruments. The system is schematically shown in Fig. (2).

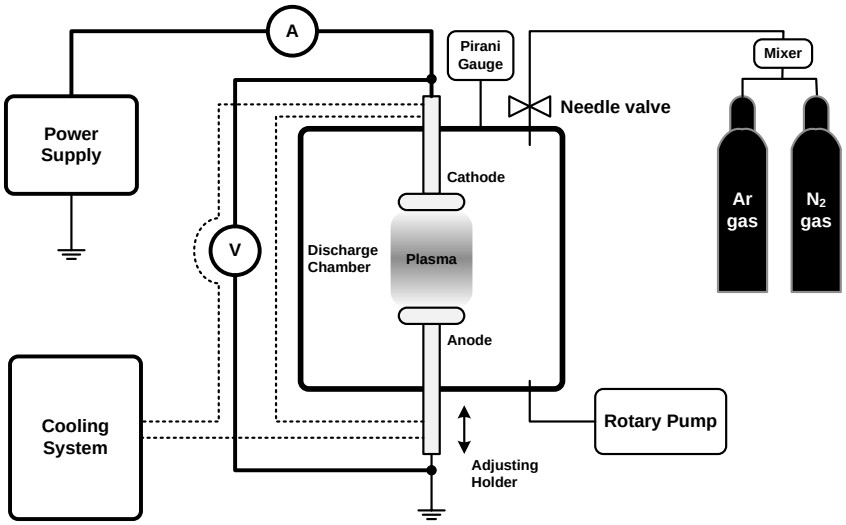

Fig. (2) Schematic diagram of the CFUDM DC sputtering system used in the present work

The vacuum chamber was constructed from stainless steel. It is a cylinder with internal diameter of 35cm, outer diameter of 45cm, and height of 37.5cm. There were four side holes of 10.8cm in diameter on the circumference of the cylinder; one of them was closed with a quartz window, while the other three were closed with glass windows. These windows were mounted by stainless steel flanges each of 21cm in diameter and four screws. They were used for monitoring the discharge and events inside the chamber. Each window was far from the discharge region by a neck of 7.5cm diameter to avoid the effects of heat developed by the glow discharge.

The vacuum chamber was sealed from lower end with a stainless steel flange of 40cm in diameter containing a feedthrough for electrical connections required for experiment. The upper end was sealed with a similar flange but containing two feedthroughs; one for gas inlet and Pirani gauge and the other for the Penning gauge. Both flanges include a central hole for the electrode hollow holder. Rubber O-rings and silicon vacuum grease were used in all sealing points.

Both discharge electrodes were constructed from stainless steel (St. St. 304) hollow disks of 80mm in diameter and 8.5mm in thickness. The electrode was joined to holder of 295mm in length and outer and inner diameters of 16.2mm and 11.6mm, respectively, to include a stainless steel channel of 78.5mm in length and 5.6mm in diameter through which the cooling water was flowed to the inside volume of the electrode. The holder tube includes a 1mm-step screw thread of 25.88mm in length to connect the cooling channel tightly.

Two permanent ring magnets were placed at the back side of each electrode to form the magnetron with a separating distance of 1cm. The inner magnet was 12.5mm in height and 31.5mm in diameter with a central hole of 17.5mm in diameter, while the outer magnet was 15.2mm in height and 80mm in diameter with a central hole of 40mm in diameter. Therefore, the two magnets were separated by a distance of 10mm around their opposing surfaces. A metallic disk of 69.7mm in diameter and 2.5mm in thickness was used to choke the outer magnet to prevent the magnetic field lines from extending to the backside of the electrode.

The design of dual magnetrons proposed in this work provides two concentric regions of high magnetic field intensity on electrode surface. At these regions, the charged particles are totally confined because the particles escaping from the inner region towards the walls of vacuum chamber will lose some energy and then be trapped by the outer region. In conventional configurations, a fraction of charged particles can escape from the confinement region and hence decrease the ionization rate near the cathode.

The advantage of magnetron on the anode is observed in the film deposition of ferromagnetic materials because the magnetic field intensity forces the deposited particles to distribute on the substrate according to its distribution. This makes possible to produce films with selective optical densities to serve multipurpose devices as in the optical data storage applications [26].

In order to prevent any variation in the arrangement of internal components, a teflon host of 100mm diameter and 44.5mm height with a central groove of 84.75mm diameter and 26.3mm depth was used

to maintain the magnetron from the backside of the electrode. This piece was locked from movement by cylindrical teflon piece of 37.5mm in diameter and 35.25mm in height containing an M5 screw driven towards the holder tube.

A single-stage rotary pump (Leybold-Heraeus) of 9 m^3/hr pumping speed was used to get pressure down to about 10^{-3} mbar inside the vacuum chamber. A water-cooled diffusion pump was available for use in this work for lower vacuum pressure and connected to the vacuum chamber via a trap. However, all results presented were obtained using the rotary pump only as vacuum pressure of 10^{-2} mbar was easily reached. The minima of Paschen's curves for the inter-electrode distances 2-6 cm were achieved at pressures higher than 10^{-3} mbar. Pirani gauge (down to 10^{-3} mbar) was used.

The flow rate of the Ar:N_2 mixture used for preparation of silicon nitride (Si_3N_4) samples was ranging between 20-50 cm^3/s.

The electrical power required for generating discharge inside vacuum chamber was provided by a 5 kV dc power supply (Edwards 2A) through high-tension cables. A current-limiting resistance (3.25 k□, 1 kW) was connected between the negative terminal of the dc power supply and the cathode inside the vacuum chamber, while the positive terminal of the dc power supply was connected directly to the anode. The output voltage of the power supply could be varied precisely over 0-5 kV to control the current flowing between discharge electrodes. However, the maximum supply voltage did not exceed 800V. Another dc power supply (0-250 V PHYWE-7532) was used to provide bias potential for Langmuir probe measurements. In addition, a third dc power supply (DHF-1502DD, 1.5-15V, 0.6-2A) was used for electrical measurements performed on the samples prepared as photodetectors.

Gas supply unit consists of argon and nitrogen cylinders, flowmeters, gas flow regulators, needle valves and connections and joints. Argon gas of 96% purity and nitrogen gas of 90% purity were used.

A compact unit was used to cool and circulate the room-temperature water through a channel in discharge electrodes. This unit can cool more than 51 liters of distilled water down to about 4°C and circulate it with maximum flow rate of 30 L/min. The temperature inside the chamber was measured by a thermometer located near the wall of the chamber while the temperatures of both electrodes were measured by thermocouples connected to digital instruments. The maximum surface temperature of the substrate placed on the anode was 40-45°C with uncooled circulating water and reasonably reduced with cooled circulating water.

The operating conditions of the system were classified into two groups; constant and variable. The constant operating conditions include inter-electrode distance, vacuum pressure, current limiting resistance, discharge voltage, discharge current, cooling temperature, cooling water flow rate and deposition time. The variable operating conditions include gas pressure and gas flow rate. Varying discharge voltage was almost possible during the operation. In addition, turning the cooling system off would raise the temperature of either electrode to 40-45°C with circulating water, while stopping the circulation of water would raise electrode temperature more (up to 150°C). More details can be found on the sputtering system and experimental setup of this work in previously published articles [27-30].

Two types of silicon wafer (n-type and p-type) were used as sputtering targets for reactive sputtering experiments using nitrogen gas. The transparent substrates used in this work were made of borosilicate glass. Before using them for sputtering experiments, they were first cleaned with ethanol to remove any oil layers or residuals may exist on their surfaces, rinsed and washed with distilled water to remove ethanol, and then dried completely before being kept in clean case or placed inside vacuum chamber. Silicon substrates of different conductivities (n-type and p-type) were cleaned by HF acid, ethanol and distilled water, dried and then used for Si_3N_4 nano films deposition.

The following measurements were carried out on the designed CFUBDM system and Si_3N_4 samples in order to characterize, classify and optimize them towards the main goal of this work. They include thickness measurements, x-ray diffraction (XRD) pattern, atomic force microscopy (AFM), scanning electron microscopy (SEM), Fourier-transform infrared spectroscopy (FTIR) and UV-Visible spectroscopy.

Thickness of the prepared samples was measured by laser-fringes method where two semiconductor lasers of 1mW output power and different wavelengths (532 and 632nm) were used to produce the concentric fringes pattern and hence calculate film thickness (d) from the following relation [31]:

$$d = \frac{L}{\Delta L} . \frac{\lambda}{2} \quad (1)$$

here L and ΔL are the widths of adjacent bright and dark fringes, respectively, and □ is the wavelength of laser beam

Using two wavelengths may make this method reasonably accurate as much as the experimental setup is carefully prepared and stabilized.

The structures of the prepared samples were analyzed with a Bruker D2 PHASER XRD system

 ISSN (print) 2958-8960 (online) xxxx-xxxx Printed in IRAQ

(Cu-Kα x-ray tube with λ=1.54056 Á). A proportional counter of 40 kV and current of 30 mA was used. The XRD patterns were recorded at a scanning rate of 0.08333°s^{-1} in 2□ ranges of 20-60°.

AFM and SPM measurements were performed on the samples prepared at the optimum conditions in order to study the surfaces of nanostructures prepared in this work as well as introduce the effects of some operating conditions on the surface of the prepared samples.

SEM measurements were performed using Tescan Vega EasyProbe instrument on samples prepared at the optimum conditions in order to confirm the formation of nanostructures as well as introduce the effects of some operating conditions on the fine structures of the prepared samples.

The FTIR measurements were carried out by FTIR spectrometer (SHIMADZU FTIR-8400S) on KBr pellets of the prepared samples.

Transmittance, absorbance and reflectance measurements of the prepared samples were carried out by using computer-controlled UV-Visible spectrophotometer (K-MAC SpectraAcademy SV-2100). This measurement process could be precisely controlled by suitable software installed on a personal computer.

3. Results and Discussion

Figure (3) shows a photograph of the Si_3N_4 films prepared at different inter-electrode distances. The minimum measured thickness is about 70nm at inter-electrode distance of 5cm.

The purity and crystallinity of the prepared Si_3N_4 nanostructures were examined by using powder x-ray diffraction (XRD) in the range of 20-60° as shown in Fig. (4). In Fig. (4a), a sharp peak belonging to pure silicon is apparently observed and some other peaks belonging to silicon dioxide (SiO_2) are also seen in addition to the formation of Si_3N_4. This may be attributed to the heat generation inside the chamber due to the higher electric power transferred to the discharge volume in absence of magnetrons, whose one of their advantages is the reduction in breakdown voltage as explained before. Therefore, some compounds (e.g., SiO_2) are induced to form at elevated temperatures inside the chamber. Pure silicon atoms appear on the substrate due to the effect of elevated temperature to remove large fraction of the nitrogen (gas) atoms from the discharge region towards cooler regions inside the chamber that prevented them from bonding to sputtered silicon atoms. These results clearly show the advantage of using magnetrons in such technique.

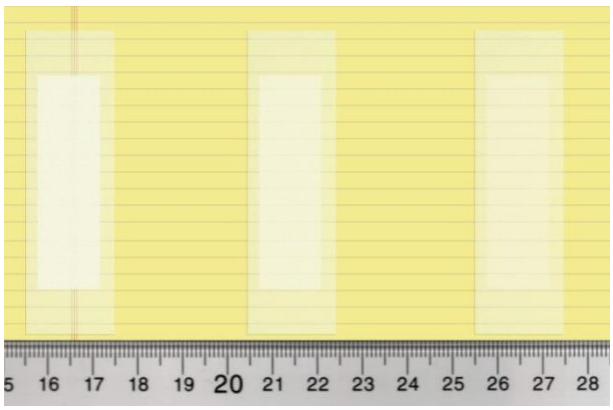

Fig. (3) The Si_3N_4 samples deposited on glass substrates at different inter-electrode distances (left to right): 2cm, 4cm and 6cm

The XRD patterns in figures (4b, c and d) explain the formation of nanostructures due to many contributions of crystal planes. At inter-electrode distance of 2cm, a sharp and high peak belonging to pure silicon is seen in addition to many small peaks belonging to nanostructured Si_3N_4. This confirms that a ratio of silicon atoms sputtered from the silicon target was not bonded to nitrogen and then deposited as pure silicon on the substrate. Increasing the inter-electrode distance to 4cm causes the sharp peak of pure silicon to disappear from the XRD pattern and only those peaks belonging to the crystal planes of Si_3N_4 nanostructures are seen. This may be attributed to increasing reaction volume between silicon and nitrogen atoms, therefore, almost all sputtered silicon atoms were bonded to nitrogen atoms to form Si_3N_4 molecules.

The most intense peaks of Si_3N_4 seen on the XRD pattern are (232), (110), (200), (321), (101) and (301) corresponding to diffraction angles of 21.0°, 23.0°, 27.0°, 32.0°, 36.0° and 52.0°, respectively, and the schematic diagrams of their crystal planes are shown in Fig. (5).

It was not easy to distinguish these peaks individually, so, it was very difficult to determine the FWHM values for these peaks and therefore the grain sizes were not determined. However, the average grain size could be precisely determined by the AFM measurements, as shown later. Table (2) includes identification parameters of Si_3N_4 indexed by the JCPDS index [32] for hexagonal structure of Si_3N_4. There are many other peaks of lower intensities seen on the XRD pattern but not included in this table.

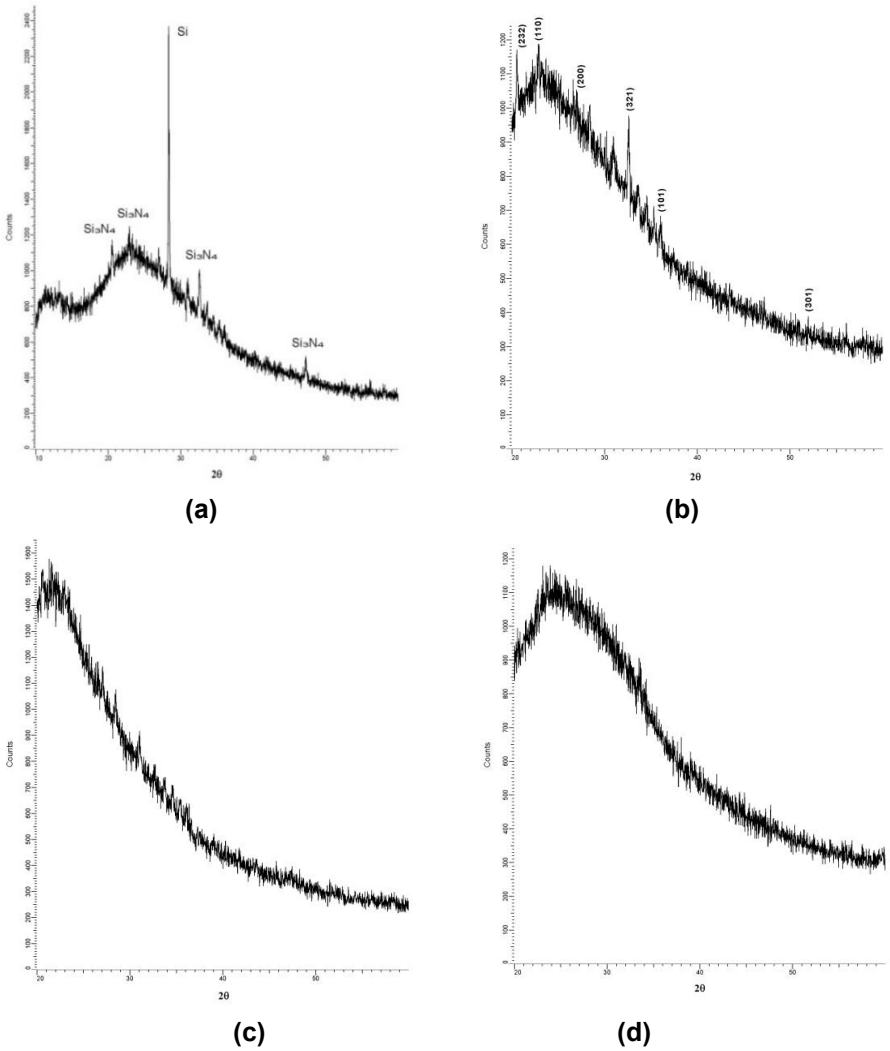

Fig. (4) The x-ray diffraction patterns of the silicon nitride samples prepared at different inter-electrode distances of (a) 4cm without magnetron(s), (b) 2cm with magnetrons, (c) 4cm with magnetrons and (d) 6cm with magnetrons

Table (2) Identification parameters of silicon nitride obtained from XRD results [32]

2θ (deg)	*d* (Å)	I/I_0	*hkl*	2θ (deg)	*d* (Å)	I/I_0	*hkl*
13.43942	6.58	42	100	41.36508	2.18	33	201
23.38007	3.80	42	110	47.75908	1.902	8	220
27.06844	3.29	100	200	48.02737	1.892	5	211
33.65061	2.66	95	101	49.85031	1.827	12	130
36.0241	2.49	95	210	52.10891	1.753	35	301
38.93992	2.31	6	111	57.8478	1.592	11	221
40.97204	2.20	5	300	59.65571	1.548	6	131

ISSN (print) 2958-8960 (online) xxxx-xxxx Printed in IRAQ

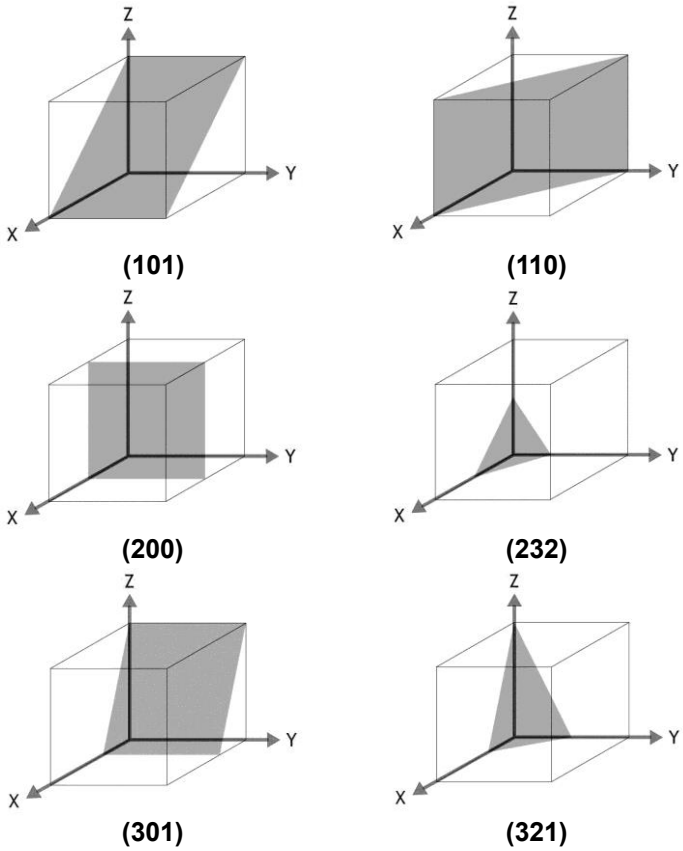

Fig. (5) Schematic diagram of some crystal planes formed in the Si_3N_4 samples

Figure (6) indicates 2D and 3D AFM images as continuous granular structure surrounded by tiny void regions is formed. The surface roughness of the prepared Si_3N_4 nanostructure is higher for the samples prepared at inter-electrode distance of 4cm and the average and R.M.S roughness were 0.777 and 1.03 nm, respectively.

Lower values of both average and R.M.S roughness are obtained in the samples prepared at smaller (2cm) and larger (6cm) distances. However, the distribution of grains over the surface was noticeably much uniform in the sample prepared at distance of 2cm compared to those prepared at larger distances. This may be attributed to the spatial disturbance effects at larger distances. Working to produce such nanostructures, higher ratio of surface area to volume is required in order to benefit from this parameter in photonic and tribology applications.

In general, homogeneous, continuous, smooth and dense Si_3N_4 nanostructures can be produced at inter-electrode distances of 2-6 cm. The loose, porous surface is directly related to columnar structures surrounded by voids and the observed transition of the film microstructure from the incompact columnar-like structure to a dense, smooth film is mainly due to the change of energetic particle bombardment during film growth. A progressive densification of the film microstructure occurs as the amount of nitrogen inside the deposition chamber is increased [33].

Figure (7) shows the SEM image of the Si_3N_4 samples prepared at different inter-electrode distances. In Fig. (7a), the Si_3N_4 nanoparticles prepared at 2cm are clustered and cannot be recognized as individual particles, while in samples prepared at 4cm (Fig. 7b), nanoparticles of 30nm in size are formed and they can be recognized as individual accumulated particles. At inter-electrode distance of 6cm (Fig. 7c), the small Si_3N_4 nanoparticles (30-35nm) are easily seen but large ones (75-100nm) are also formed at the lower layers of the structure.

The formation of clusters in samples prepared at 2cm is attributed to the higher rate of deposition as the continuously formed nanoparticles are located on other nanoparticles already positioned on the substrate; i.e., they do not find empty positions and are forced to cluster with other nanoparticles.

For the samples prepared at 4cm, the deposition rate is decreased and Si_3N_4 nanoparticles may have good opportunity to locate on the substrate as those coming later may find empty locations to deposit on instead of accumulate over deposited ones. However, continuously produced Si_3N_4 nanoparticles may not find locations to deposit; therefore, they have formed new layers of nanoparticles but with reasonable recognition.

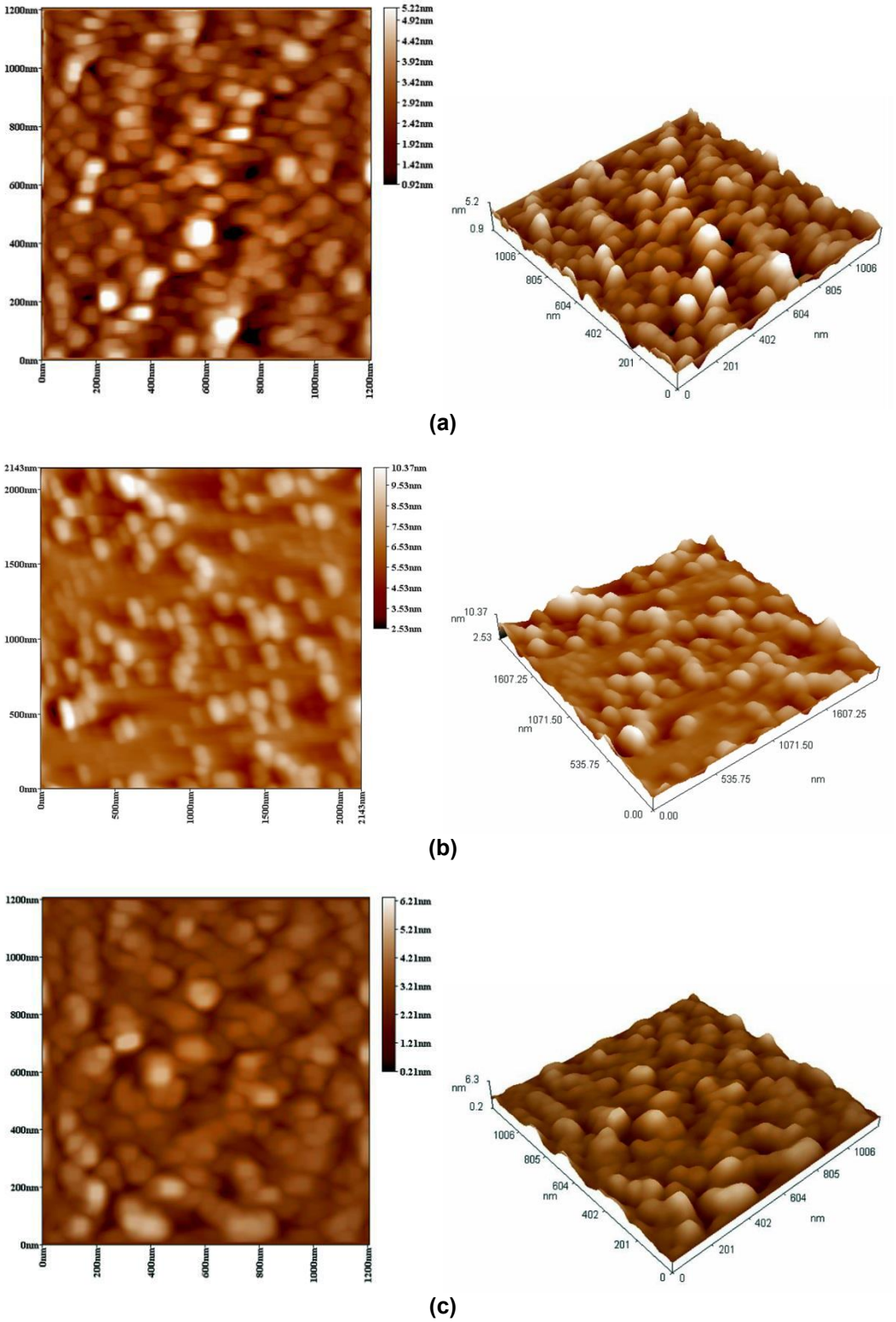

Fig. (6) AFM micrographs of the silicon nitride nanostructures prepared at inter-electrode distance of (a) 2cm, (b) 4cm and (c) 6cm

For the sample prepared at 6cm, the deposition rate is much decreased and the distribution of the Si_3N_4 nanoparticles on the substrate is inhomogeneous. This is attributed to the effects of thermodynamics and fluid mechanics because a fraction of the formed nanoparticles are lost towards the walls of the chamber. The formation of big particles (75-100nm) may be attributed to the tendencies of Si_3N_4 nanoparticles to merge and form larger particles as these Si_3N_4 nanoparticles

have many different crystal planes and they could geometrically combine.

Due to their excellent property in forming protective barriers against the diffusion of some ions in the surrounding environment, the cluster structures of Si_3N_4 nanoparticles may be preferred for this purpose. Whereas photonic applications may require structures like those prepared at distances larger than 4cm to benefit from the properties of Si_3N_4 nanoparticles as individual as possible. High-temperature and tribology applications may require structures of larger particle sizes as their contact surfaces are at the minimum.

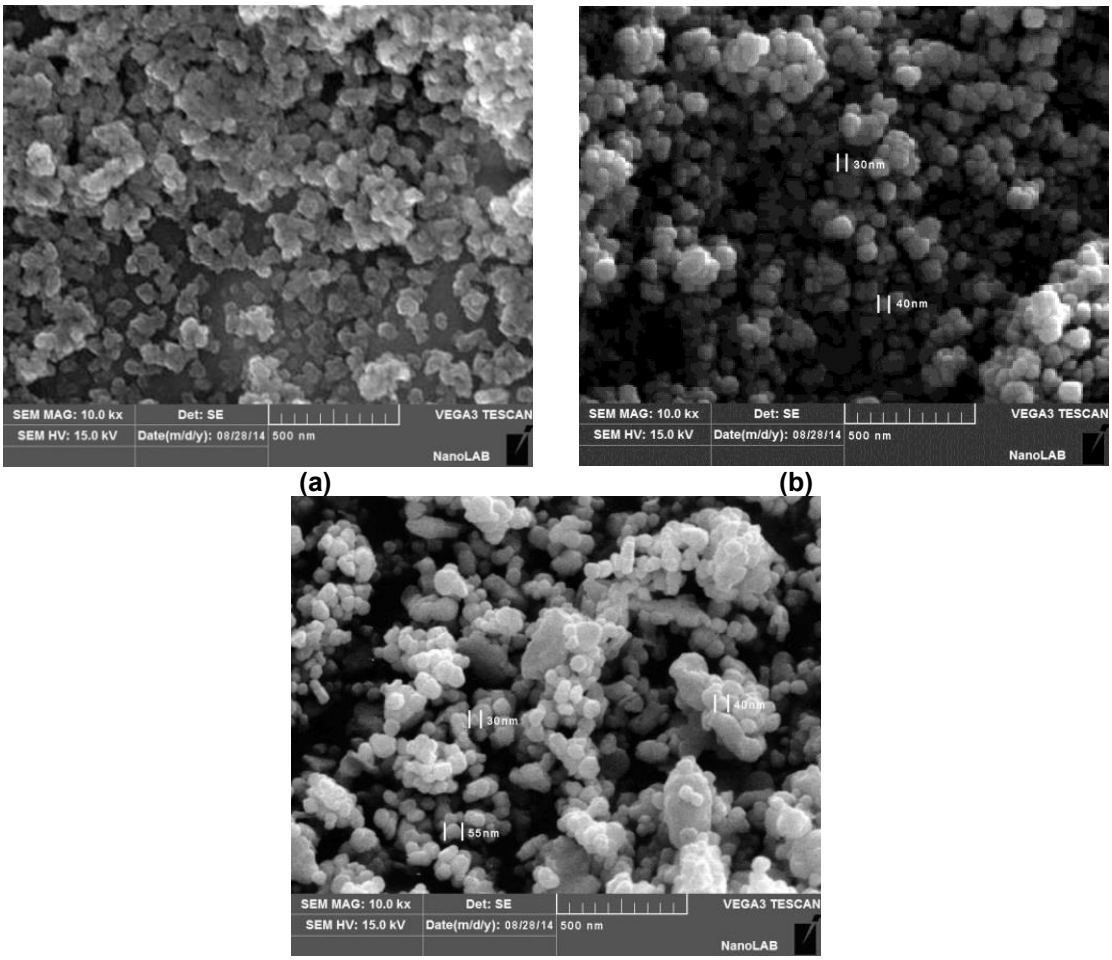

Fig. (7) SEM micrographs of the silicon nitride nanostructures prepared at different inter-electrode distances of (a) 2cm, (b) 4cm and (c) 6cm

The FTIR spectrum of Si_3N_4 nanostructures is shown in Fig. (8), where two bands of significant absorption can be seen around 960 and 1086 cm^{-1}. These bands are attributed to the Si-N-Si vibration mode in Si_3N_4 molecule [34]. These broad bands indicates that the structure of Si_3N_4 include nanocrystals.

The absorption peaks seen around 460 cm^{-1} are attributed to the formation of SiO_2 [35]. Other absorption peaks seen at 1400-3600 cm^{-1} may be attributed to the presence of some contaminations formed on the Si_3N_4 samples when exposed to air. A characteristics feature of silicon nitride is its strong reactivity when exposed to air or humidity, so the surface region of Si_3N_4 film (or powder) has a significant amount of Si_2-NH, Si-NH and Si-OH groups [36].

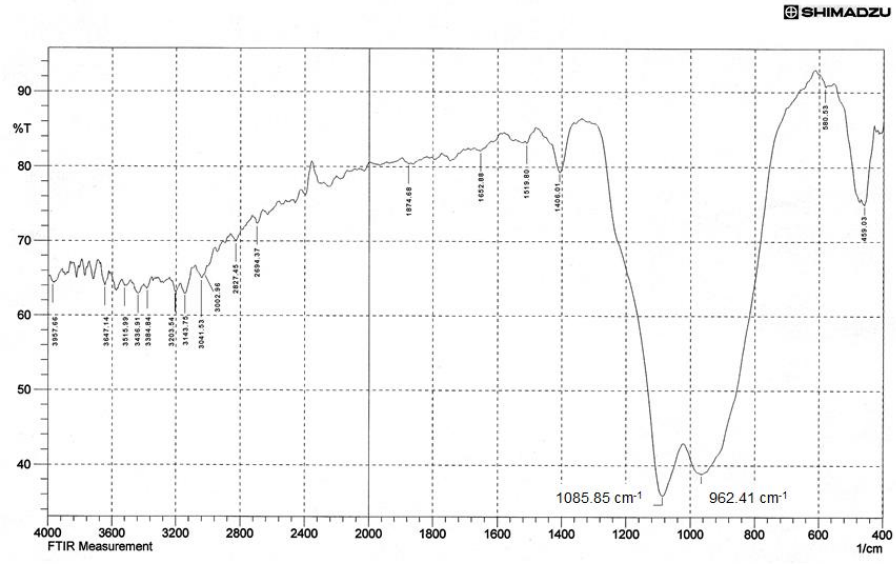

Fig. (8) FTIR of the Si_3N_4 samples prepared at inter-electrode distance of 4cm

Transmission and absorption spectra of the prepared samples were measured in order to determine the spectral behavior of them over different spectral regions (UV and visible) as well as calculate their optical constants, such as absorption coefficient, value and type of energy band gap, and refractive index. Figures (9) and (10) show these spectra.

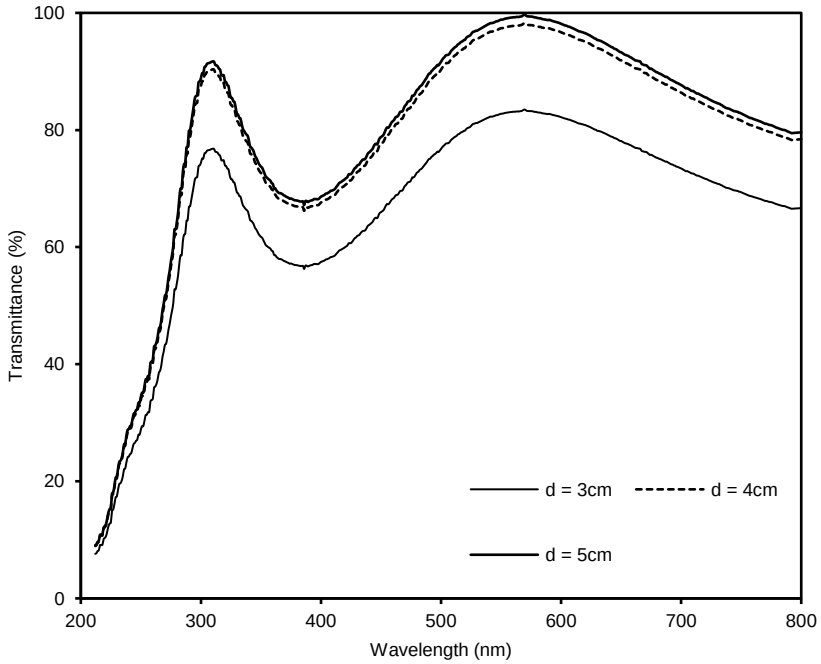

Fig. (9) Transmission spectra of Si_3N_4 films prepared at different distances

The transmittance of the prepared Si_3N_4 nanostructures is low in the UV region shorter than 250nm and it increases to first peak at 300-305nm before decreasing again. Beyond 400nm, the transmittance increases to its maximum (completely transparent for samples prepared at 4 and 5cm) at 560-570nm. Transmittance decreases in the NIR region (beyond 800nm). There are two peaks in the region 300-600nm and one minimum at 389nm and this behavior is attributed to the quantum size effect of nanostructures [37].

As shown in Fig. (10), the Si_3N_4 nanostructures highly absorb in UV region and highly transmit in the visible region with a small region near 380-390nm where the absorbance has a relatively low peak, which may be a motivation to fabricate photodetectors from Si_3N_4 nanostructures at this narrow band of UV wavelengths.

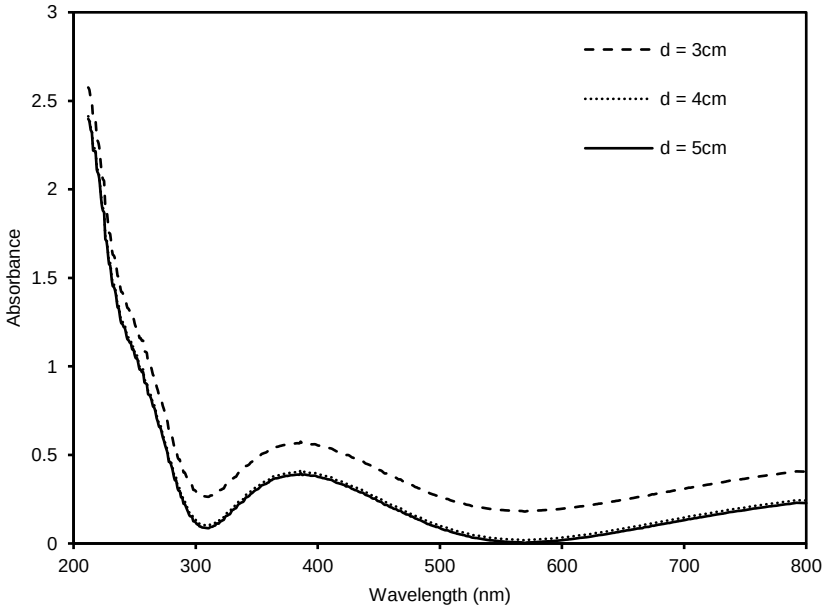

Fig. (10) Absorbance spectra of silicon nitride films prepared at different inter-electrode distances

Depending on the transmission spectra of the prepared Si_3N_4 film samples, the refractive index was calculated by the Swanepoel formula [31]. Accordingly, the value of refractive index is found to be 1.38-2.1.

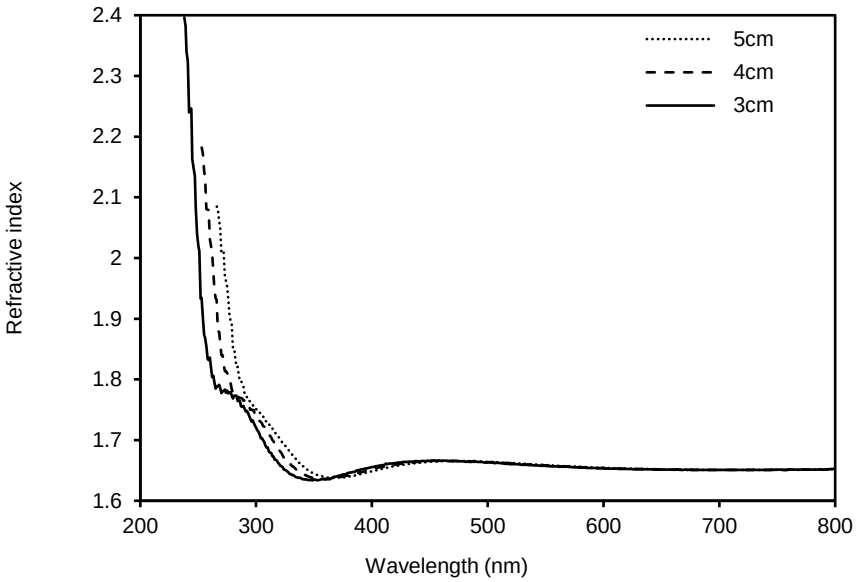

Fig. (11) Dispersion relation for the silicon nitride samples prepared at different inter-electrode distances

In order to introduce the homogeneity of the prepared samples in the visible region of electromagnetic spectrum, the dispersion relation was plotted for these samples as shown in Fig. (11).

Due to high absorption in the UV region, the refractive index has high values at wavelengths shorter than 250nm, while it drastically decreases before entering the region of visible wavelengths, in which it has approximately constant values. This confirms the homogeneity of the prepared samples.

The energy band gap (E_g) of the Si_3N_4 samples prepared at inter-electrode distances of 3, 4 and 5cm was determined as shown in Fig. (12). According to the relation between (□h□)^2 and h□, the energy band gap is direct allowed and ranging in 5.1-5.2 eV.

As shown in Fig. (13), the energy band gap is increasing with increasing the inter-electrode distance because the thickness of the prepared structure is accordingly decreased. The wide energy band gap of Si_3N_4 nanostructures makes it good candidate, as similar as AlN, BN and GaN, for power electronics and optoelectronics operating at high temperatures.

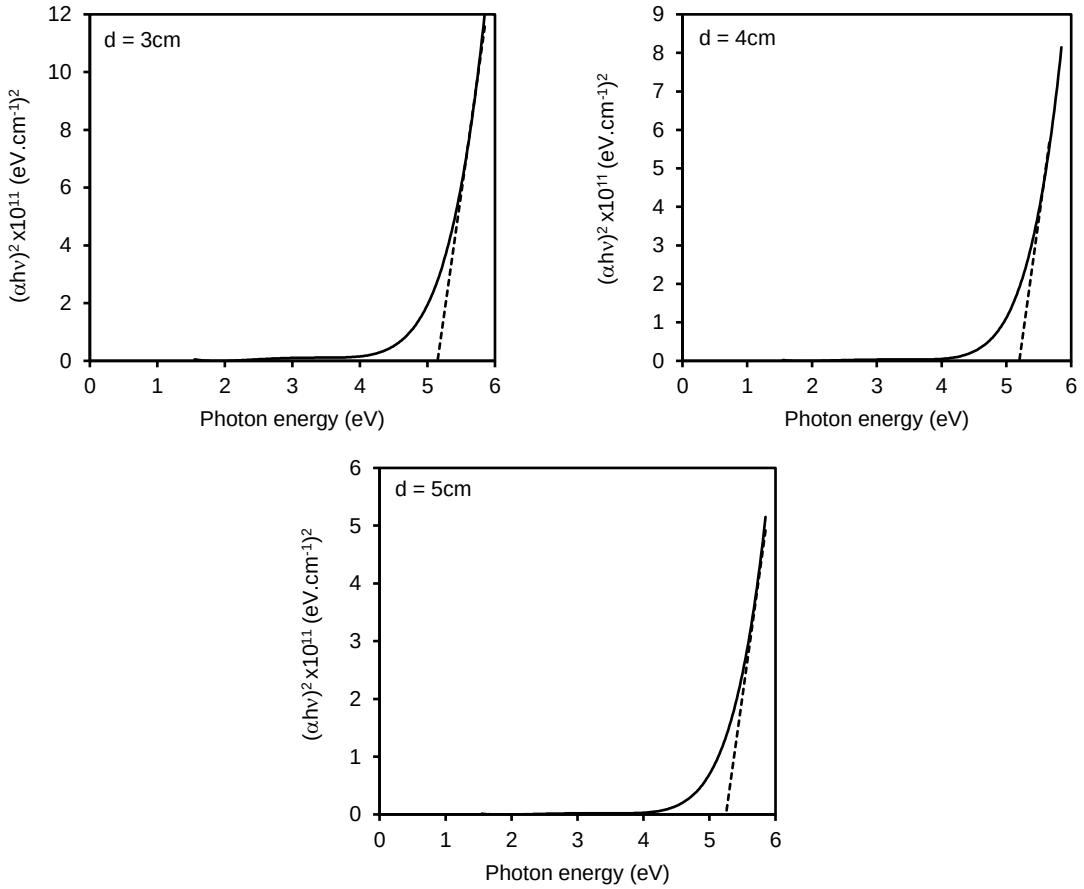

Fig. (12) Determination of energy band gap of the Si_3N_4 samples prepared at different inter-electrode distances (E_g = 5.12-5.28 eV)

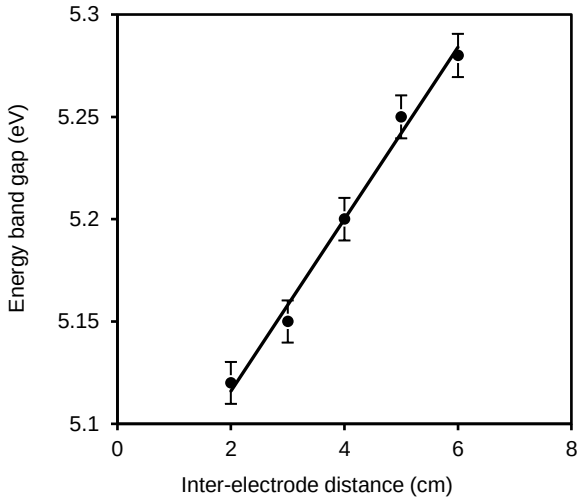

Fig. (13) Variation of energy band gap of the prepared Si_3N_4 samples with inter-electrode distance

4. Conclusion

In this work, novel design of closed-field unbalanced dual magnetrons system was employed in a DC reactive sputtering system to prepare silicon nitride nanostructures. The prepared nanostructured were polycrystalline with six dominant crystal planes: (101), (110), (200), (232), (301) and (321). The surface roughness of the sample prepared at inter-electrode distance of 4cm was higher than other samples prepared at smaller or larger distances and the average and R.M.S roughness were 0.777 and 1.03 nm, respectively. The nanoparticles of minimum size of 30nm were formed and recognized as individual accumulated particles. An absorption peak was observed at 389nm, which is attributed to the quantum size effect of nanostructures. The refractive index of the prepared Si_3N_4 samples was determined to be 1.38-2.1 and the energy band gap was ranging in 5.1-5.2 eV. The energy band gap was found to increase with decreasing thickness of the prepared film. The wide energy band gap of Si_3N_4 nanostructures makes them good candidate for power electronics and optoelectronics operating at high temperatures.

References

[1] M. Ohring, The Materials Science of Thin Films, Academic Press, p. 79, 112 (1992).
[2] D. Huy Trinh, Nanocrystalline Alumina-Zirconia Thin Films Grown by Magnetron Sputtering, Linköping University, Sweden, p. 1 (2008).
[3] K. Wasa, M. Kitabatake, H. Adachi, Thin Film Materials Technology: Sputtering of Compound Materials, William Andrew Inc., p. 139, 116, 2, 119, 72, 106, 103, 9 (2004).
[4] D.R. Gibson, Deposition of multilayer optical coatings using closed field magnetron sputtering, online article (2006).
[5] J.C. da Conceição Lorenzzi, Boron nitride thin films deposited by magnetron sputtering on Si_3N_4, PhD thesis, Universidade de Aveiro, Departamento de Engenharia Cerâmica e do Vidro, pp. 10-16 (2007).
[6] Yu.G. Dobrovolskiy, V.L. Perevertailo and B.G. Shabashkevich, Anti-reflection coatings based on SnO_2, SiO_2, Si_3N_4 films for photodiodes operating in UV and visible spectral ranges, Semicond. Phys., Quantum Electron. & Optoelectron., 14(3), 298-301 (2011).
[7] Bharat Bhushan (Ed.), Springer Handbook of Nanotechnology, Springer, p. 27, 151, 438 (2004).
[8] S. Leitch, Spectroscopic Analysis of Selected Silicon Ceramics, M.Sc. thesis, University of Saskatchewan (Canada) (2005), p. 16.
[9] B. Liu, Atomic-scale studies of native point defect and nonstoichiometry in silicon oxynitride, J. of Phys. and Chem. of Solids, 70, 982–988 (2009).
[10] N. Maluf and K. Williams, An Introduction to Microelectromechanical Systems Engineering, Artech House, Inc., p. 19, 39 (2004).
[11] P.M. Martin, Handbook of Thin Film Deposition Techniques, Elsevier, p. 4 (2010).
[12] X. Zhang and C.P. Grigoropoulos, Thermal conductivity and diffusivity of free-standing silicon nitride thin films, Rev. Sci. Instrum., 66(2), 1115-1120 (1995).
[13] I. Safi, Recent aspects concerning DC reactive magnetron sputtering of thin films: A review, Surf. Coat. Technol., 127, 203-219 (2000).
[14] Wei-Tang Li, Effect of sputtering-gas pressure on properties of silicon nitride films produced by helicon plasma sputtering, Thin Solid Films, 384, 46-52 (2001).
[15] M. Vila, D. Cáceres and C. Prieto, Mechanical properties of sputtered silicon nitride thin films, J. Appl. Phys., 94(12), 7868-7873 (2003).
[16] Gang Xu, Optical investigation of silicon nitride thin films deposited by r.f. magnetron sputtering, Thin Solid Films, 425, 196–202 (2003).

[17] S.A. Awan and R.D. Gould, Conductivity and dielectric properties of silicon nitride thin films prepared by RF magnetron sputtering using nitrogen gas, Thin Solid Films, 423, 267–272 (2003).
[18] Zh.Q. Yao, Composition, structure and properties of SiNx films fabricated by pulsed reactive closed-field unbalanced magnetron sputtering, Nuclear Instrum. And Methods in Phys. Res., B240, 741–751 (2005).
[19] K. Mokeddem, M. Aoucher and T. Smail, Hydrogenated amorphous SiN deposited by DC magnetron sputtering, Superlattices and Microstructures, 40, 598–602 (2006).
[20] Zh.Q. Yao, Studies of the composition, tribology and wetting behavior of silicon nitride films formed by pulsed reactive closed-field unbalanced magnetron sputtering, Nuclear Instrum. And Methods in Phys. Res., B242, 33–36 (2006).
[21] Yu Xiang, Investigation of Ti/TiN multilayered films in a reactive mid-frequency dual-magnetron sputtering, Appl. Surf. Sci., 253, 3705–3711 (2007).
[22] A. Batan, Characterisation of the silicon nitride thin films deposited by plasma magnetron, Surf. Interface Anal., 40, 754–757 (2008).
[23] Asim Aijaz, Dual-magnetron open field sputtering system for sideways deposition of thin films, Surf. Coat. Technol., 204(14), 2165-2169 (2009).
[24] B. Ganguli, High density plasma beam source for nitriding, Indian J. of Pure & Appl. Phys., 49, 759-764 (2011).
[25] M.A. Signore, Deposition of SiN thin films by RF magnetron sputtering: a material and growth process study, Optical Materials, 34, 632–638 (2012).
[26] Sankar M. Borah, Direct Current Magnetron Glow Discharge Plasma Characteristics Study for Controlled Deposition of Titanium Nitride Thin Film, J. of Materials, vol. 2013, article ID 852859.
[27] O.A. Hammadi, M.K. Khalaf, F.J. Kadhim, B.T. Chiad, “Operation Characteristics of a Closed-Field Unbalanced Dual-Magnetrons Plasma Sputtering System”, Bulg. J. Phys., 41(1), 24-33 (2014).
[28] O.A. Hammadi, M.K. Khalaf, F.J. Kadhim, “Fabrication of UV Photodetector from Nickel Oxide Nanoparticles Deposited on Silicon Substrate by Closed-Field Unbalanced Dual Magnetron Sputtering Techniques”, Opt. Quantum Electron., 47(12), 3805-3813 (2015). DOI: 10.1007/s11082-015-0247-6
[29] O.A. Hammadi, M.K. Khalaf, F.J. Kadhim, “Fabrication and Characterization of UV Photodetectors Based on Silicon Nitride Nanostructures Prepared by Magnetron Sputtering”, Proc. ImechE, Part N, J. Nanoeng. Nanosys., 230(1), 32-36 (2016). DOI: 10.1177/1740349915610600
[30] O.A. Hammadi, M.K. Khalaf, F.J. Kadhim, “Silicon Nitride Nanostructures Prepared by Reactive Sputtering Using Closed-Field Unbalanced Dual Magnetrons”, Proc. ImechE, Part L, J. Mater.: Design and Applications, 231(5), 479-487 (2017), DOI: 10.1177/1464420715601151.
[31] Salwan K. Al-Ani, Methods of Determining the Refractive Index of Thin Solid Films, Iraqi J. Appl. Phys., 4(1), 17-23 (2008).
[32] JCPDS 1979, C 29-1133, Joint Committee on Powder Standards, International Center for Diffraction Data, USA (1979)
[33] Olivier Debieu, Structural and optical characterization of pure Si-rich nitride thin films, Nanoscale Res. Lett., 8, 31, (2013).
[34] V.P. Tolstoy, I.V. Chernyshova and V.A. Skryshevsky, Handbook of Infrared Spectroscopy of Ultrathin Films, John Wiley & Sons, Inc. (NJ), p. 435 (2003).
[35] N.N. Greenwood and E.J.F. Ross, Index of Vibrational Spectra of Inorganic and Organometallic Compounds, vol. I, Butterworth Group (London), p. 326, 328 (1960).
[36] N.N. Greenwood and E.J.F. Ross, Index of Vibrational Spectra of Inorganic and Organometallic Compounds, vol. II, Butterworth Group (London), p. 457 (1963).
[37] N.N. Greenwood and E.J.F. Ross, Index of Vibrational Spectra of Inorganic and Organometallic Compounds, vol. III, Butterworth Group (London), p. 800, 1078 (1966).

 ISSN (print) 2958-8960 (online) xxxx-xxxx Printed in IRAQ